Tuned AFM-FM coupling by the formation of vacancy complex in Gd0.6Ca0.4MnO3 thin film lattice

Beiranvand, A.; Liedke, M. O.; Haalisto, C.; Lähteenlahti, V.; Schulman, A.; Granroth, S.; Palonen, H.; Butterling, M.; Wagner, A.; Huhtinen, H.; Paturi, P.;

Originally published:

May 2021

Journal of Physics: Condensed Matter 33(2021), 255803

DOI: https://doi.org/10.1088/1361-648X/abf9ba

Tuned AFM–FM coupling by the formation of vacancy complex in $Gd_{0.6}Ca_{0.4}MnO_3$ thin film lattice

A. Beiranvand[1], M. O. Liedke[2], C. Haalisto[3], V. Lähteenlahti[1], A. Schulman[1], S. Granroth[3], H. Palonen[1], M. Butterling[2], A. Wagner[2], H. Huhtinen[1] and P. Paturi[1]

[1] Wihuri Physical Laboratory, Department of Physics and Astronomy, University of Turku, FI-20014 Turku, Finland

[2] Helmholtz-Zentrum Dresden–Rossendorf, Institute of Radiation Physics, Bautzner Landstraße 400, 01328 Dresden, Germany

[3] Laboratory of Materials Science, Department of Physics and Astronomy, University of Turku, FI-20014 Turku, Finland

E-mail: azabei@utu.fi

November 2020

Abstract. The effect of *in situ* oxygen and vacuum annealings on the low bandwidth manganite $Gd_{1-x}Ca_xMnO_3$ (GCMO) thin film with $x = 0.4$ was investigated. Based on the magnetic measurements, the AFM–FM coupling is suppressed by the vacuum annealing treatment via destroying the double exchange interaction and increasing the unit cell volume by converting the Mn^{4+} to the Mn^{3+}. Consequently, resistance increases significantly compared to pristine film. The results are explained by a model obtained from the positron annihilation studies, where the vacuum annealing increased the annihilation lifetime in A and B sites due to the formation of vacancy complexes $V_{A,B} - V_O$, which was not the case in the pristine sample. The positron annihilation analysis indicated that most of the open volume defects have been detected in the interface region rather than on the subsurface layer and this result is confirmed by detailed x-ray reflection analysis. On the other hand, the effect of oxygen annealing on the unit cell volume and magnetization was insignificant. This is in agreement with positron annihilation results which demonstrated that the introduction of oxygen does not change the number of cation vacancies significantly. This work demonstrates that the modification of oxygen vacancies and vacancy complexes can tune magnetic and electronic structure of the epitaxial thin films to provide new functionalities in future applications.

1. Introduction

The doped perovskite oxide manganites ($L_{1-x}A_xMnO_3$, where L and A are trivalent lanthanide and divalent alkaline earth ions, respectively) have become the focus of extensive research because they can readily show the different electronic phases by proper substitution of cations [1, 2, 3, 4, 5]. Manganites contain different types of

interactions that are comparable in strength. As a result, they can have distinct phases like ferromagnetic (FM) metal, a charge-ordered (CO) insulator or a paramagnetic (PM) insulator depending on which of the interactions are won over [6]. Robustness or suppression of the interactions in the manganite thin films can be affected by different factors such as film thickness [7, 8, 9], lattice and substrate induced strain [10, 11, 12] and oxygen variation [13, 14, 15]. Oxygen concentration plays a key role in variation of Mn–O–Mn bond angle and in Mn^{4+}/Mn^{3+} ratio, which both can affect on the electronic and manganite phase diagram [15, 16, 17]. The double-exchange (DE) interaction between Mn^{3+} and Mn^{4+} ions via the intermediate oxygen ion [18] leads to ferromagnetic (FM) metallic or insulating phase, whereas the superexchange [19] interaction between Mn^{3+}–Mn^{3+} and Mn^{4+}–Mn^{4+} leads to antiferromagnetic (AFM) insulating phase. Furthermore, the existence of oxygen vacancies, V_O, on the surface, interface and the bulk of various oxide materials can give rise to intriguing insights for potential opportunities of practical applications [20]. In order to achieve the integration of oxide based electronic devices, there is a strong stimulus to control of oxygen content during the growth of high-quality oxide thin films. The *in situ* procedure is a technique to control the oxygen content. For example, an oxygen deficiency can be produced by annealing in the vacuum while an oxygen excess in oxygen atmosphere.

Among the perovskite manganites, the low-bandwidth manganites are especially interesting due to their stable CO state in the large doping range and resistive switching feature [21]. The earlier investigation of $Gd_{1-x}Ca_xMnO_3$ (GCMO) phase diagram as a bulk and as a film in the whole range of Ca concentrations [22, 23] demonstrated that the GCMO films not only show the CO/OO state near room temperature in the middle range of Ca substitution, but also metallic conductivity appeared in high Ca concentrations. These properties motivated us to explore the effect of oxygen variation on structural, electrical and magnetic properties. In the present paper, we report the effect of *in situ* oxygen and vacuum treatments on GCMO films with $x = 0.4$ Ca concentration grown by pulsed laser deposition technique through structural, electrical and magnetic characterization. We also investigate how the treatments affect the defect types and on the vacancy concentrations in these films.

2. Experimental methods

The epitaxial GCMO films were grown on $SrTiO_3$ (STO) substrates by pulsed laser deposition (PLD). 2000 pulses of XeCl-laser ($\lambda = 308$ nm) with the energy density of 1.3 J/cm^2 and frequency of 5 Hz were used for the depositions of all samples. The deposition temperature was 700 °C and after the deposition the films were kept at the atmospheric pressure of oxygen for 10 min at 700 °C, before cooling them down to room temperature (pristine film). Details of the target preparation and the film deposition parameters have been reported elsewhere [22, 21]. In order to control the oxygen content of the films and to affect the valency of Mn ions, the different *in situ* annealing treatments were done for the pristine films. For oxygen treatment, after deposition, the films were

kept at the atmospheric pressure of oxygen for 60 min at 700 °C, before cooling them down to room temperature. For vacuum treatment, after the deposition, the films were kept in vacuum of 10^{-4} Torr for 10 min at 600 °C before cooling them down to room temperature. All the GCMO films grow diagonally on STO substrate.

The structural properties of the thin films were explored using a Philips Empyrean diffractometer with a 5-axis goniometer and Pixcel 3D detector. $\theta - 2\theta$ scans over $(00l)$, $(0hl)$ and (khl) peaks and 2-dimensional $\phi - 2\theta$ scan of (224) peak were done to determine the lattice parameters with the Nelson–Riley method [24]. The thickness of the GCMO layer and interface layer were determined by performing x-ray reflectivity measurements (XRR). The x-ray photoelectron spectroscopy (XPS) spectra were obtained with Thermo Scientific Nexsa system. The spectra were collected using monochromated Al Kα radiation and dual beam charge compensation. 50 eV pass energy was used to scan the core-level spectra. Vacancy like defects and their relative concentrations were determined by positron annihilation spectroscopy. The details of the experiment is given in the supplementary file. The temperature dependence of the zero-field-cooled (ZFC) and the field-cooled (FC) magnetizations were measured between temperatures of 10 and 400 K with a Quantum Design SQUID magnetometer in 50 mT external magnetic field. The magnetic hysteresis curves were recorded in magnetic fields up to 5 T at temperatures of 10, 50, 100 and 400 K. The external field B was always oriented along the GCMO (110) axis in the plane of the films. The resistivity measurements were done with the constant current of 0.5 μA at temperature range from 10 to 400 K and magnetoresistance measurement at 10 K in magnetic fields up to 9 T were made with the Physical Property Measurement System (PPMS, Quantum Design)

3. Results and discussion

3.1. Structural and electronic properties

The $\theta-2\theta$ scans of all films showed only GCMO $(00l)$ and substrate peaks. No diffraction peaks from secondary phases are observed, which means that all the films are single phase and have a preferential orientation (Fig 1). It is clearly seen that the vacuum annealing treatment causes the peaks to shift in $(00l)$, $(0hl)$ and (khl) directions to the lower 2θ values, which results in larger lattice parameters compared to the pristine sample. However, the shift is not significant for the oxygen treated film. Similarly to the pristine film, the oxygen treated film shows a shoulder in (002) and (004) peaks (see the inset of Fig. 1a). In order to understand this splitting, the $2\theta - \phi$ scans of GCMO(224) peak were measured (not shown here). The sharp peaks of (224) at the positions expected and the narrow peaks in (004) directions displayed that the films are fully textured and c-axis orientated, without evidence of twin boundaries. Therefore, we can conclude that the shoulders could be related to the relaxation of the strained layer next to the film-substrate interface, which has earlier been observed in other perovskite films [25, 26, 27].

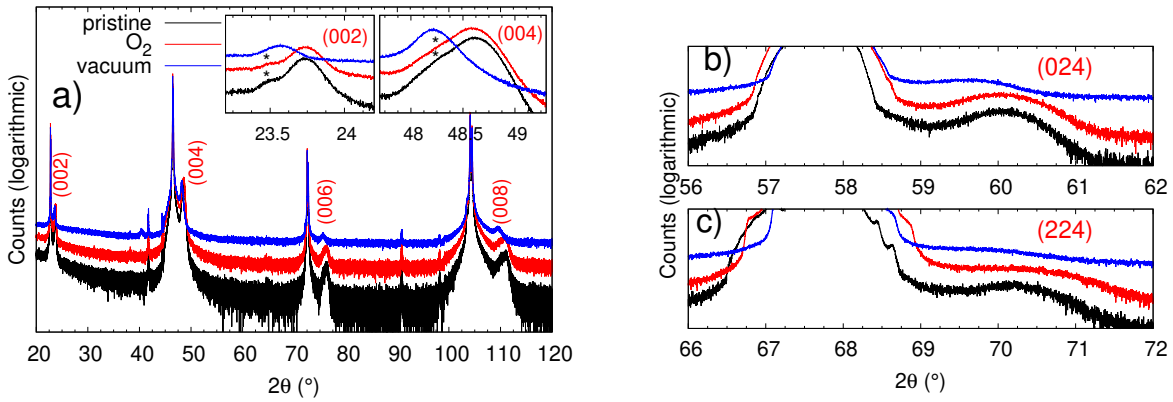

Figure 1. The room temperature XRD patterns of GCMO films grown on STO substrate with different annealing treatments in a) (00l) and b) (0hl) and c) (khl) directions. The insets are the closer views of (002) and (004) peaks and the curves are shifted for clarity. The shoulders marked with an asterisk (*) arise from the strain.

The lattice parameters and the peak widths (FWHM) were determined from the 2θ scans of (004), (024) and (224) peaks. The values are listed in Table 1. The 2θ FHWM values for (004) peak and the peak width in ϕ direction for (224) peak decrease for vacuum treated film, while they are the same for oxygen treated as in the pristine film. This indicates that the vacuum treated film has lower variation in the lattice parameter in the c direction and smaller number of low-angle grain boundaries in comparison with pristine film.

Table 1. Lattice parameters, lattice mismatch between GCMO films and substrate along the a and b directions, unit cell volume, 2θ peak width measured from (004) peak and ϕ peak width from (224). The thickness of the GCMO film (D_{film}), interface (D_{int}) and surface (D_{sur}) and the roughness of the surface (r) of all the films are extracted from XRR measurements at room temprature

$x = 0.4$	*XRD* data			*XRR* data			
	pristine	O_2-annealed	vacuum-annealed		pristine	O_2-annealed	vacuum-annealed
a (Å)	5.43	5.38	5.45	D_{film} (nm)	57	55	35
b (Å)	5.40	5.40	5.42	D_{int}(nm)	7	4	23
c (Å)	7.5	7.50	7.55	D_{sur}(nm)	<1	1	12
ε_a (%)	0.018	0.026	0.013	r (nm)	2.8	0.8	3.7
ε_b (%)	0.021	0.022	0.02				
V_{cell} (Å^3)	219.84	218.06	223.02				
FWHM θ(°)	0.56	0.51	0.33				
FWHM ϕ(°)	2.89	2.7	2.15				

In comparison with the pristine film, it can be seen that the out-of-plane lattice parameter remains almost unchanged within experimental errors while the in-plane lattice parameters shrink in a direction with oxygen annealing, slightly decreasing the unit cell volume (see Table 1). This is well explained by the replacement of Mn^{3+} with

larger ionic radius (0.07 nm) by Mn^{4+} with smaller ionic radius (0.05 nm), causing a shorter cation-oxygen-cation bond length compared with the cation-cation bond [18]. On the other hand, adding oxygen atoms in MnO_6 octahedron increases 1/6 of the oxygen atomic radius in the unit cell volume. In the competition between two processes, the former one is prominent and therefore the increase of oxygen content leads to the decrease of the unit cell volume. However, lattice parameters are elongated in both the out-of-plane and in-plane directions with vacuum annealing, which is followed by the increase of unit cell volume. The increase of the unit cell size is probably due to conversion of the smaller Mn^{4+} ions to the larger Mn^{3+} ions, as has been reported earlier in literature [16, 28, 17].

Fig. 2 plots the measured XRR patterns for GCMO/STO films with different annealings and the corresponding fit by using GenX software [29]. A four-layer model composed substrate (STO), interface, GCMO film and a surface layer provided the best fitting for the all films. The thickness of the films, as well as the roughness of the surface and interface are extracted from the fitting and shown in Table 1. According to previous reports [30, 31, 32], existence of interface between substrate and films in addition to the lattice mismatch between film and the substrate can be due to defects. Shimoyama *et al.* [33, 31] reported that, when $BaTiO_3$, $PbTiO_3$ and $SrTiO_3$ doped with RE components are epitaxially grown on STO substrate in low pressure of oxygen, the oxygen of the films automatically fed from the substrate during the deposition (shows schematic in Fig. 2b). Therefore, we can say that, in the GCMO pristine film, the interface probably attributed to the mismatch and oxygen vacancies accumulated in the STO substrate surface. In the vacuum annealed film, although the film has the smallest lattice mismatch, the thickness of the interface layer increases significantly compared to the pristine film. It seems that the role of defect concentration in the interface thickness dominate and the vacuum treatment introduces more oxygen vacancies in both GCMO film and the substrate (STO), when compared to the pristine one. However, decreasing the concentration of oxygen vacancies with oxygen annealing leads to a thinner interface layer. The details of the open volume defect concentration in the interface will be discussed in the following section.

The thickness and the roughness of the surface layer are $<$1 nm and 2.8 nm respectively for the pristine film and these values change to 1 nm and 0.8 nm respectively for the oxygen treated film. It seems that the annealing process partially increases the oxygen concentration at the film surface resulting also in smoother surface in comparison with pristine one. In contrast, the thicker and rougher surface layer have been obtained from XRR measurement for vacuum annealed film (12 nm thickness and 3.7 nm roughness). As published earlier [34, 35], removing oxygen from the surface by the vacuum treatment could increase roughness in the film surface.

XPS measurements were performed for the all the films. The survey spectra and the core levels of Mn 2p, Mn 3s, O 1s, Gd 3d, Ca 2p and C 1s were obtained. The binding energy of C 1s was used to calibrate the binding energy scale of all core level spectra. No satellite peaks in the Mn 2p spectra were detected for any of the samples,

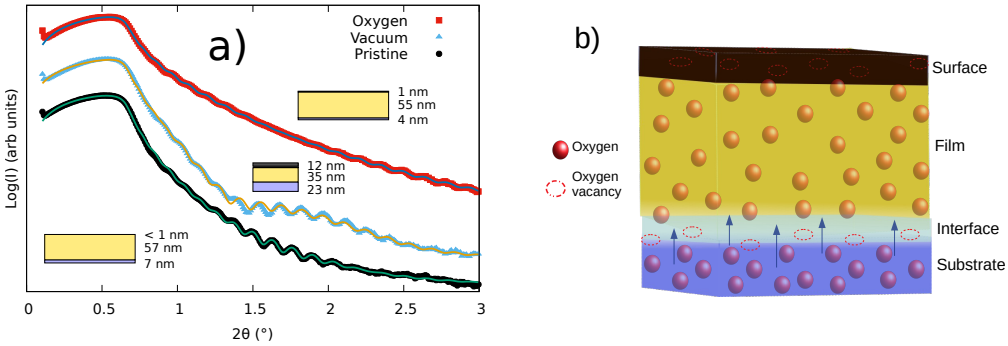

Figure 2. The experimental (filled symbols) and simulated (solid lines) XRR data from GCMO films with oxygen and vacuum annealing as well as pristine sample. The data and simulated curves are artificially shifted upwards for clarity. b) The schematic view of travelling oxygen from substrate to film and accumulating oxygen vacancies in the interface and surface.

which means that Mn^{2+} is not present in these films. The binding energies and the shapes of the core levels in the pristine and the oxygen treated films were similar. No significant differences were observed in all the core level spectra. In the mixed valence manganites, a broad Mn $2p_{3/2}$ peak around 642 eV binding energy and missing Mn^{2+} satellite feature at around 648 eV indicates an overlap of Mn^{3+} $2p_{3/2}$ and Mn^{4+} $2p_{3/2}$ peaks, which can be attributed to the coexistence of Mn^{3+} and Mn^{4+} ions [36, 37, 38]. Therefore, in our measurements, we can interpret that Mn $2p_{3/2}$ peak forms from both Mn^{3+} and Mn^{4+} ions. A closer view of this peak shows a narrower peak with slight shift to the lower binding energy side for vacuum annealed sample when compared with pristine and oxygen treated samples, indicating an increase in the number of Mn^{3+} ions with vacuum treatment (Fig. 3). As expected from the increase of oxygen vacancies.

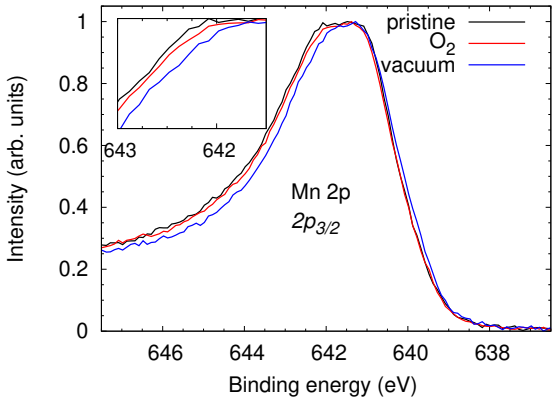

Figure 3. The Mn $2p_{3/2}$ core level XPS spectra of pristine, O_2-treated and vacuum-treated GCMO films. The main panel displays the peaks at binding energy around 642 eV. The inset shows closer view from the higher binding energy side of the peaks in order to reveal the detailed differences of Mn valencies.

3.2. Defect formation by positron annihilation spectroscopy

In order to study the defect types in GCMO films, positron annihilation spectroscopy (PAS) and positron annihilation lifetime spectroscopy (PALS) techniques have been used. In PAS measurement, S (low electron momentum fraction) scales proportionally with concentration and/or defect size. This is shown as a function of positron annihilation energy, E_P in Fig. 4. The mean implantation depth of positron is shown by the upper horizontal axis. The S values are constant at E_P>6 keV, indicating that in this energy range, almost all positrons are implanted into the substrate and annihilated with bulk states. For the GCMO vacuum annealed film, the strong increase of S for E_P<5 keV suggests higher defect concentration and likely larger defects size compared to the pristine and oxygen annealed films. The possible candidate can be the oxygen vacancies (V_O) in the reduced oxygen atmosphere. The similar results have been published earlier for PAS studies of other perovskite materials [32, 39] where vacuum annealing was used as a redox factor. The S values for pristine and oxygen treated films are the same within the experimental errors, which means that the oxygen treatment does not have effect on V_O concentration. The proper interpretation is that the single V_O is positively charged or at best neutral, hence repelling positrons or of low affinity to positrons, respectively. It is known that if oxygen vacancies are positively charged in the pristine film, the concentration of vacancies remains the same after oxygen annealing [40].

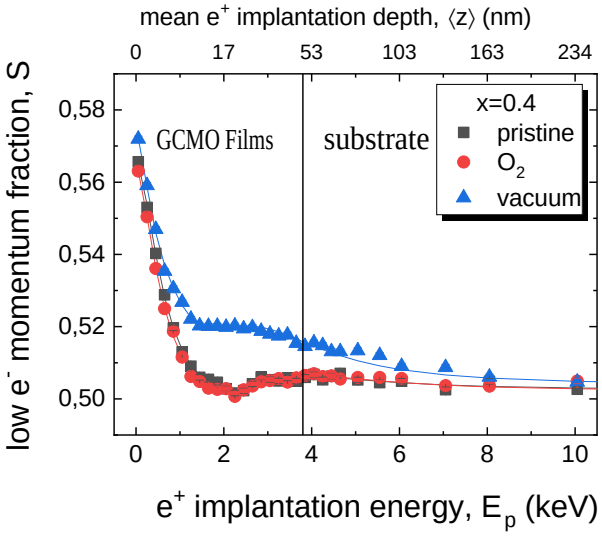

Figure 4. S parameter (low electron momentum fraction) as a function of positron implantation energy E_p and mean positron implantation depth z_{mean}. The solid curves show the results of fitting under assumption that the density and overall thickness of the film layer and substrate are constant.

For the analysis of positron diffusion length, L_+, which is inversely proportional to the defect concentration, the VEPFit code has been utilized [41]. The method permits to fit $S(E_p)$ curves for multilayered systems and to acquire thickness T_i, effective positron diffusion length $L_{+,i}$, and specific S_i-parameters for layer i within a stack. The calculated

S_i, T_i, and $L_{+,i}$ are presented in Table 2. The overall thickness of the films were obtained from XRR measurements. The material densities for GCMO have been theoretically calculated for the perfect unit cell. The density ρ and the positron diffusion length, L_+, of STO substrate were determined from the uncoated substrate (ρ_{STO}=5.11 g.cm^{-3} and L_+=11 nm) and they were considered constant during the fit for all samples. $S(E_p)$ curves for pristine and O_2 treated samples exhibit a rather pronounced maximum at the E_p range of about 3–5 keV and show a broader maximum for vacuum annealed film. It is usually an indication of additional defect state in the interface region [42] and hence a fitting procedure requires an additional layer to explain the maximum. It will be shown that such a layer is strongly defected when compared to the upper part of the film (see Table 2). The fitting procedure allows the precise estimation of the both layer thicknesses, T, as well as their diffusion lengths, L. Two characteristic regions were found across the film thickness for all the samples, revealing a different defect microstructure: (i) the sub-surface region with relatively low defect concentration and (ii) interface region showing greater number of open volume defects. For the GCMO films, the defect concentration decreases (L_+ increases) in the subsurface region in case of O_2 and vacuum treated samples, whereas in the interface region the opposite behaviour is observed. From the data in Table 2, in the interface region not only the defect concentration is strongly increased in the vacuum treated film, but the calculated thickness is doubled when compared to the pristine one (increasing from 12 nm for the pristine to approx. 23 nm for the vacuum treated film).

Table 2. The parameters calculated from the positron lifetime measurements for differently treated GCMO thin films.

Sample	S_1	T_1 (nm)	$L_{+,1}$ (nm)	S_2	T_2 (nm)	$L_{+,2}$ (nm)
pristine	0.498(5)	43(1)	5.4(4)	0.517(1)	12	1
O_2-annealed	0.495(6)	43.4(9)	6.9(4)	0.521(1)	8.6	0.4
vacuum-annealed	0.485(3)	25(1)	11.8(5)	0.539(3)	23	0.1–0.2
Sample	$\tau 1$ (ps)	I_1 (%)	$\tau 2$ (ps)	I_2 (%)		
pristine	185	78	320	22		
O_2-annealed	180	77	300	20		
vacuum-annealed	210	88	360	10		

To obtain more straightforward explanation for different defect types, the positron lifetime measurements have been done. The lifetime spectrum measured at room temperature was decomposed into two components, $\tau 1$ and $\tau 2$. The lifetime values and their intensities for all samples are listed in Table 2. The short lifetime component $\tau 1$ represents vacancy annihilation in B-site (V_B) and a longer lifetime component $\tau 2$, reflects the vacancies in the A-site or grain boundaries. In the GCMO case, V_B could be vacancy in Mn site and V_A could be related to Gd or Ca vacancies. The DFT calculations exhibit that the lifetime spectroscopy in the range of 150–160 ps is for perfect lattice, 190–200 ps for the six-coordinated B-site monovacancy and 280–290 ps for 12-coordinated A-site monovacancy. Typical values of positron lifetimes in perovskite oxides can be found in [43, 44, 45]. The values for GCMO materials could be similar

to that of complex perovskites such as $BaTiO_3$, $PbTiO_3$ and $SrTiO_3$ doped with RE components [46, 43, 32]. For the GCMO system with 0.4 Ca concentration $\tau 1 \approx$ 164–180 ps with 78 % intensity, which could be related to the vacancy in the Mn site. The lifetime increases to 210 ps with 88 % intensity after vacuum annealing in both the film and substrate regions. It is probably due to the formation of vacancy complex V_O–V_B in GCMO and the substrate. The effect of oxygen treatment is insignificant on size and the concentration of Mn vacancies in the GCMO. Hence, it can be attributed to the positively charged single oxygen vacancies, however it cannot be directly shown with the PAS. The positron annihilation lifetime measurement shows the second decomposition, $\tau 2$ = 300–320 ps with about 20 % intensity, for pristine sample which is close to the lifetime values in the A-site vacancies (Gd or Ca vacancies in the present work). This value is somewhat larger than the theoretical value for A-site monovacancy [44, 46]. One possible interpretation is that the observed lifetime is not only due to the isolate Gd or Ca vacancies but also other open volume defects should be considered. $\tau 2$ increases as the oxygen content is decreased by vacuum annealing treatment. This could be attributed to the formation of V_O–$V_{Gd,Ca}$ complex. However, in the vacuum annealed film, the intensity I_2 decreases 10 % in comparison with the pristine sample, which means that the defect concentration is likely smaller in this film. This is in agreement with the narrower XRD peaks in ϕ direction for vacuum treated film when compared to the pristine and oxygen annealed films. It means that the vacuum annealed sample has lower concentration of low-angle grain boundaries compared to the pristine and oxygen annealed samples. As discussed above, $\tau 2$ positron lifetime is due to mixed of $V_{Gd,Ca}$ and other defects like low-angle grain boundaries. Hence, the lower concentration of low-angle grain boundaries can lead to lower intensity I_2.

3.3. Magnetic and electrical properties

The effect of annealing treatments on the magnetic and electrical properties of GCMO (x = 0.4) films was investigated using the field and temperature dependent magnetization and resistance measurements. Magnetization and resistance measurements as a function of temperature of all the films were performed in zero-field-cooled (ZFC) and field-cooled (FC) mode by applying a static magnetic field of 50 mT and 9 T ,respectively, in a wide range of temperature from 10 to 400 K (Fig. 5). From ZFC curves, all the films show a ferromagnetic background at low temperature. The net magnetic moment at low temperature in GCMO samples is mainly due to magnetic momentum of Gd, which is oriented along the external magnetic field and antiparallel to Mn moments. In the warming process, the Mn magnetic moments dominate and maximum around 50 K. Such a behaviour has been reported in previous literature [23, 47, 48]. This transition exhibits ferromagnetic (FM) alignment in competition with antiferromagnetic alignment of Mn ions. The transition shows lower values of magnetization in vacuum annealed sample in comparison with the pristine one, but the effect of oxygen annealing on the transition is insignificant. Based on the XPS results, it

could be suggested that the oxygen/vacuum treatment increases/decreases the content of Mn^{4+} leading to improved/suppressed FM double-exchange interaction compared to the case of as-grown film.

The magnetic interaction between the Mn ions in mixed valence perovskites can be explained by double exchange (DE) and superexchange (SE) mechanisms. Both mechanisms need oxygen as an intermediate, meaning that the spins of the Mn ions interact with each other indirectly through the oxygen ion [18]. Apparently, the increase of V_O/V_O–V_B vacancy concentration can lead to rotation and tilting of the oxygen octahedra [49], which undoubtedly influences the hybridization between Mn 3d and O 2p orbitals via the variations of the Mn–O–Mn bond lengths and angles (see Fig. 5b). Furthermore, one oxygen ion can share two electrons and change the valence of Mn ions, which means that some Mn^{3+} cations transform into Mn^{4+}. As shown in the simplified illustration in Fig. 5c, the neighboring Mn cations with different valences (Mn^{3+} and Mn^{4+}) favor the FM configuration via double exchange interaction, while the Mn cations neighboring with the same valence, favor the AFM configuration via the superexchange interaction. Therefore, a relatively high concentration of oxygen or oxygen complex (V_B–V_O) vacancies could stabilize the AFM state over FM state, thus decreasing the magnetic moment. This is in agreement with the positron annihilation results, which showed higher concentration of oxygen and oxygen complex vacancies in vacuum annealed film in comparison with pristine one.

In FC curves, the ferromagnetic to paramagnetic transition has been observed at Curie temperature (T_C) for all samples and the T_C determined from the first derivative of FC magnetization dM/dT is around 63 K for all films. Based on the previous reports [17, 11, 50], we expected that the vacuum annealed sample with greater number of oxygen vacancies should show lower T_C when compared with the pristine sample, but in this set of samples, T_C is roughly the same for all of them. According to the literature, introduction of oxygen vacancies and tensile strain decreases T_C. This discrepancy can be explained so that the vacuum treated sample has the narrowest ϕ peak, indicating smaller number of low-angle grain boundaries. In addition, it has the smallest expansive in-plane lattice mismatch between the film and the substrate among the films (see Table 1). These two features could explain the increase of T_C, as also reported earlier [7, 51].

The hysteresis loops of all the films were measured up to 5 T at 10 and 50 K. The saturation magnetization M_s is slightly higher for the oxygen treated film and it is the lowest for the vacuum annealed film when compared to the pristine sample, indicating more/lower FM volume fraction due to oxygen vacancy concentration in oxygen/vacuum annealed samples (Table 3). Similar to the typical AFM $M(H)$ curves, the magnetization increases linearly with field and it does not saturate below 5 T for any of the films. This confirms the appearance of FM state within the AFM matrix in these films. The coercive field, H_C, calculated from hysteresis loops at 50 K, for pristine and oxygen annealed films is roughly the same $\approx$12.5 mT, but for vacuum treated film H_C is greater $\approx$25 mT. As reported before, the defects such as oxygen vacancies and, on the other hand, AFM–FM coupling can pin the domain wall movement, resulting

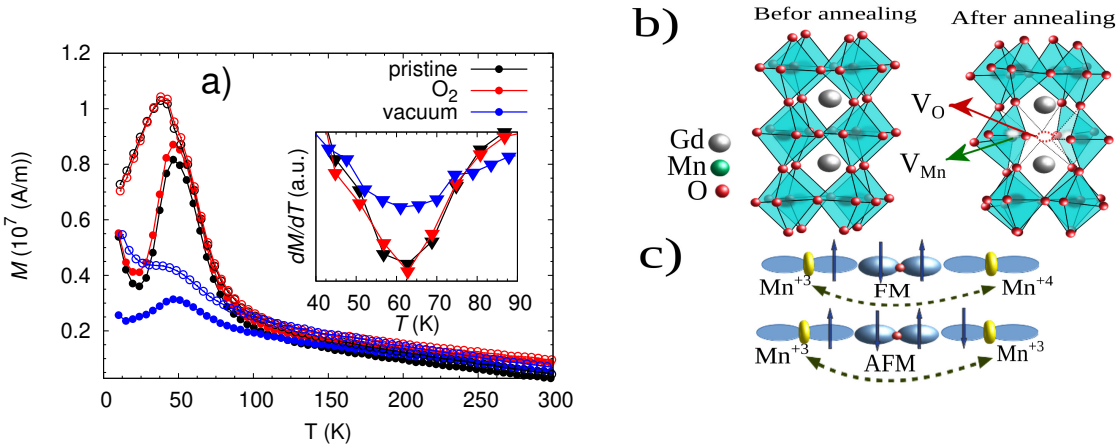

Figure 5. a) The temperature dependences of ZFC and FC magnetization curves measured in 50 mT. ZFC curves are shown with filled symbols and FC curves with open symbols. The inset shows the temperature dependence of the first derivative dM/dT of the FC magnetization, where the peak position corresponds to T_C. b) The simple schematic of the perovskite structure unit cell, before and after treatment, where the red dotted circles denote oxygen vacancies and green dotted circles Mn vacancies. c) Schematic illustration of the mechanism, showing that the oxygen has a significant influence on the Mn–O–Mn orbital hybridization through the double exchange and superexchange interactions.

in increased H_C in manganites [52, 53]. In GCMO ($x = 0.4$) case, it seems that the oxygen vacancies or other defects has greater impact on coercive field than to the AFM–FM coupling. Therefore, the vacuum treated sample with more oxygen vacancies shows broader hysteresis loop when compared with oxygen treated and pristine samples, having stronger AFM–FM coupling and greater number of grain boundaries.

Table 3. The magnetic parameters of the films: T_C is the Curie temperature, $M(5T)$ is the magnetization at 50 K and 5 T and H_C is the coercive field at 50 K. R_{300} is resistivity at room temperature.

Sample	$M(5T)$ (10^8 A/m)	H_C (Oe)	T_C (K)	R_{300} (kΩ)
pristine	1.5	125	63	3
O_2-annealed	1.7	124	63	2
vacuum-annealed	0.65	250	64	35

In addition to the magnetization, the transport properties of GCMO films are investigated. Fig. **??** shows the temperature dependence of resistivity ($R(T)$) of pristine and annealed films. For the all samples, the resistivity increases gradually as temperature decreases indicating insulating behaviour. $R(T)$ curves for the pristine and oxygen samples are similar. However, the resistivity increases significantly by vacuum annealing treatment and the magnitude in room temperature is about 10 times larger than that of the pristine sample (Table 3). In such a complex manganites, the resistivity depends on Mn^{3+}/ Mn^{4+} ratio and oxygen content which makes a bridge moves electron

between Mn ions [17, 11]. Hence, decreasing this ratio and oxygen content by vacuum treatment lead to increase resistivity. The resistivity results are in agreement with the interpretation made based on the magnetic measurements.

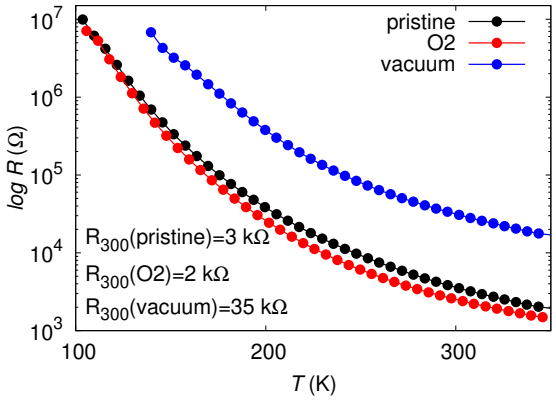

Figure 6. The $R(T)$ curves of pristine, O_2-treated and vacuum-treated GCMO films. R_{300} is resistivity in room temperature. The data below 100 K is cut due to the large noise of the device

4. Conclusion

We investigated the effect of oxygen content in GCMO thin films grown on STO substrate by *in situ* annealing in oxygen and vacuum atmospheres. We show that by introducing more oxygen vacancies to the GCMO lattice, the AFM–FM coupling is suppressed by reduction of the ferromagnetic DE interaction. This also increases the in-plane lattice parameters, resulting in smaller lattice mismatch between the GCMO film and the substrate. The positron annihilation studies indicate that both the oxygen and vacuum treatments decrease the defect concentration in sub–surface layer but increase it in the interface layer. In addition, the lifetime of annihilation is longer in A and B sites for the vacuum annealed sample, which can be explained, together with X-ray reflection measurements, by the formation of vacancy complexes in the GCMO thin films lattice. Our results present valuable insights and non-trivial profile of oxygen vacancies and vacancy complex contributions in these components which may provide a guidance in material choice for the actual memory devices.

Acknowledgments

The authors wish to thank the Jenny and Antti Wihuri Foundation, Finland and Academy of Finland project 308285. AB also acknowledges the Väisälä foundation for financial support. The authors also are grateful to E. Hirschmann and A. G. Attallah for their technical assistance in positron annihilation measurements.

References

[1] Martin C, Maignan A, Hervieu M and Raveau B 1999 *Phys. Rev. B* **60** 12191
[2] Goto T, Kimura T, Lawes G, Ramirez A P and Tokura Y 2004 *Phys. Rev. Lett.* **92**
[3] Hcini S, Boudard M, Zemni S and Oumezzine M 2014 *J. Ceram. Int* **40** 16041–16050
[4] Liu C J, Bhaskar A and Yuan J J 2011 *Appl. Phys. Lett.* **98** 214101
[5] Sarkar T, Ghosh B and Raychaudhuri A K 2008 *Phys. Rev. B* **77** 235112
[6] Rao C and Raychaudhuri A 1998 *Colossal Magnetoresistance, Charge Ordering and Related Properties of Manganese Oxides* (World Scientific)
[7] Wang H S, Wertz E, Hu Y F and Li Q 2000 *J. Appl. Phys.* **87** 7409
[8] Nemes N M, García-Hernández M, Szatmári Z, Fehér T and Simon F 2008 *IEEE Transaction on Magnetic* **44** 2926
[9] Jin S, Tiefel T H, McMormack M, OBryan H M, Chen L H, Ramesh R and Schurig D 1995 *Appl. Phys. Lett.* **67** 557
[10] Guo H, Burgess J, Street S and Gupta A 2006 *Appl. Phys. Lett.* **89** 022509
[11] Lee Y P and Park S Y 2004 *Appl. Phys. Lett.* **84** 777
[12] Rao R A, Lavric D, Nath T K and Eom C B 1998 *Appl. Phys. Lett.* **73** 3294
[13] Sirena M, Haberkorn N, Granada M, Steren L and Guimpel J 2004 *J. Magn. and Magn. Mater.* **272-276** 1171
[14] Zhao Y G, Cai W, Zhao J, Zhang X P, Cao B S, Zhu M H, Zhang L W, Ogale S B, Wu T and Venkatesan T 2002 *Phys. Rev. B* **65** 144406
[15] Klenov D O, Donner W, Foran B and Stemmer S 2003 *Appl. Phys. Lett.* **82** 3427
[16] Majumdar S, Huhtinen H, Granroth S and Paturi P 2012 *J. Phys. Cond. Mat.* **24** 206002
[17] Trukhanov S V, Troyanchuk I O and Korshunov F P 2001 *J. Low Temp. Phys.* **27** 283
[18] Goodenough J B 1955 *Physical Review* **100** 564
[19] Jahn H A and Teller E 1937 *Proc. R. Soc. A* **161** 220–235
[20] Song C, Malik I A, Li M, Zhang Q, Wang L, Wang J, Chen R, Zheng R, Dong S, Gu L, Duan W, Nan C W and Zhang J 2019 *Sci. China Mater.* **62(4)** 577–585
[21] Paturi P, Tikkanen J and Huhtinen H 2017 *J. Magn. and Magn. Mater.* **432** 164 –168
[22] Beiranvand A, Tikkanen J, Huhtinen H and Paturi P 2017 *Journal of Alloys and Compounds* **720** 126–130
[23] Beiranvand A, Tikkanen J, Huhtinen H and Paturi P 2018 *J. Magn. and Magn. Mater.* **10** 1016
[24] Nelson J B and Riley D P 1945 *Proc. Phys. Soc.* **57** 160
[25] Jeong D and Dho J 2010 *J. Appl. Phys.* **46** 1883
[26] Song J H, Kim K, Oh Y, Jung H J, Song J, Choi D K and Choi W 2001 *Journal of Crystal Growth* **223** 129
[27] Salvato M, Vecchione A, Santis A D, Bobba F and Cucolo A M 2005 *J. Appl. Phys.* **97** 103712
[28] Liu B, Liu G, Feng H, Wang C, Yang H and Wang Y 2016 *Materials and Design* **89** 715–720
[29] Björck M and Andersson G 2007 *J. Apple. Cryst.* **40** 1174–1178
[30] Herger R, Willmott P R, Schlepütz C M, Björck M, Pauli S A, Martoccia D and Patterson B D 2008 *Phys. Rev. B* **77** 085401
[31] Shimoyama K, Kiyohara M, Uedono A and Yamabe K 2002 *Jpn. J. Appl. Phys.* **41** L269
[32] Uedono A, Shimayama K, Kiyohara M, Chen Z Q and Yamabe K 2002 *J. Appl. Phys.* **92** 2697
[33] Shimoyama K, Kubo K, Maeda T and Yamabe K 2001 *Jpn. J. Appl. Phys.* **40** L463
[34] Li F, Zhan Y, Lee T H, Liu X, Chikamatsu A, Guo T, z H J Lin, Huang J C A and Fahlman M 2011 *J. Phys. Chem. C* **115** 16947–16953
[35] Wang C, j Jin K, Gu L, b Lu H, m Li S and j Zhou W 2013 *Appl. Phys. Lett.* **102** 252401
[36] Felhi H, Smari M, Bajorek A, Nouri K, Dhahri E and Bessais L 2019 *Progress in Natural Science: Materials International* **29** 198–209
[37] Gao J, Dai S Y and Li T K 2003 *Phys. Rev. B* **67** 153403
[38] Beyreuther E, Grafström S, Eng L M, Thiele C and Dörr K 2006 *Phys. Rev. B* **73** 155425

[39] Uedono A, Kiyohara M, Yasui N and Yamabe K 2005 *J. Appl. Phys.* **97** 033508
[40] Puska M J, Corbel C and Nieminen R M 1990 *Phys. Rev. B* **41** 9980
[41] van Veen A, Schut H, Clement M, de Nijs J M M, Kruseman A and Ijpma M R 1995 *Appl. Surf. Sci.* **85** 216
[42] Kosub T, Kopte M, Hühne R, Appel P, Shields B, Maletinsky P, Hübner R, Liedke M O, Fassbender J, Schmidt O G and Makarov D 2017 *Nature Communications* **8** 13985
[43] Keeble D J, Wicklein S, Dittmann R, Ravelli L, Mackie R A and Egger W 2010 *Phys. Rev. Lett.* **105** 226102
[44] Mackie R A, Singh S, Laverock J, Dugdale S B and Keeble D J 2009 *Phys. Rev. B* **79** 014102
[45] Keeble D J, Singh S, Mackie A, Morozov M, McGuire S and Damjanovic D 2007 *Phys. Rev. B* **76** 144109
[46] Ghosh V J, Nielsen B and Friessnegg T 1999 *Phys. Rev. B* **61** 207
[47] Pena O, Bahout M, Ghanimi K, Duran P, Gutierrez D and Moure C 2002 *J. M. Chemistry* **12** 2480–2485
[48] Ma Y, Viry M G, Barahona P and Pena O 2005 *Appl. Phys. Lett.* **86** 062506
[49] Liao Z, Huijben M and Zhong Z 2016 *Nature Materials* **15** 425–431
[50] Millis A J, Darling T and Migliori A 1998 *J. Appl. Phys.* **83** 1588
[51] Saloaro M, Deniz H, Huhtinen H, Palonen H, Majumdar S and Paturi P 2015 *J. Phys. Cond. Mat.* **27** 386001:1–11
[52] Bessais L, Sab S, Djega-Mariadassou C, Dan N H and Phuc N X 2004 *Phys. Rev. B* **70** 134401
[53] Prellier W, Simon C, Haghiri-Gosnet A M, Mercey B and Raveau B 2000 *Phys. Rev. B* **62** R16337